Detection of broken rotor bars in induction motor using starting-current analysis and effects of loading

R. Supangat, N. Ertugrul, W.L. Soong, D.A. Gray, C. Hansen and J. Grieger

Abstract: The detection of broken-rotor-bar faults based on common steady-state-analysis techniques, such as the fast Fourier transform (FFT), is known to be significantly dependent on the loading conditions of the induction motor. At light load, it is difficult to distinguish between healthy and faulty rotors because the characteristic broken-rotor-bar fault frequencies in the stator current are very close to the fundamental-frequency component and their amplitudes are small in comparison. As a result, detection of broken bar faults and classification of the fault severity under light load is very difficult. To overcome this problem, the analysis of the envelope of the transient starting-current waveform using the wavelet-transform has been investigated. The envelope extraction is used to remove the strong fundamental-frequency component, which would otherwise overshadow the characteristic differences between a healthy motor and a faulty motor with broken rotor bars. The wavelet-transform results are processed to develop a normalised parameter called the 'wavelet indicator' which is sensitive to the presence of broken-rotor-bar faults. The results are verified using tests on machines with a varying number of broken bars, as well as partially broken rotor bars, over a wide range of loading conditions. The effects of initial rotor position and supply imbalance are also investigated.

1 Introduction

Induction motors are generally reliable and require minimum maintenance. However, like other motors, they eventually deteriorate and fail. This gives rise to the need for cost-effective preventive maintenance based on condition monitoring, which can be addressed by monitoring and analysing the real-time signals of the motors.

There has been a substantial amount of research over the past 15 years on the development of various steady-state condition monitoring techniques, which are mainly based on the fast Fourier transform (FFT) [1–6]. FFT analysis is usually applied when the motor is operating in the steady state. A set of measurements is taken over a period of time and is analysed to obtain the signal frequency components, where the frequency resolution is both determined and limited by the measurement period.

Broken rotor bars are one of the easiest induction-motor faults to detect using steady-state stator current condition monitoring. This is based on monitoring the amplitudes of the double slip-frequency sidebands of the fundamental supply frequency in the current spectrum [3]. It has been shown that, the greater the rotor-bar-fault severity, the higher is the amplitude of these sidebands. However, the sideband amplitudes are also sensitive to motor loading [1–6]. For example, at no load or at very light loads, these broken-rotor-bar sidebands are undetectable owing to the small rotor currents experienced under this condition. Therefore, there is a pressing need to develop condition-monitoring techniques to address these issues and hence allow effective detection of rotor faults at light loads.

During direct-on-line (DOL) starting, the rotor current of the induction machine is very high, typically 5–6 times rated current. Under these conditions, rotor faults should be much more evident than under normal running conditions. There is also the advantage that the starting current is less sensitive than the running current to the level of motor load, and so reliable conclusions from the data analysis should be obtainable even with motors with no mechanical load. The two drawbacks in dealing with the starting current are first that the motor speed is constantly changing during starting, which means that the fault-related-signal frequency components are changing in both amplitude and frequency, and secondly that the starting current only occurs for a short time. The starting time, which depends on the total inertia of the motor and the load, may vary from a fraction of a second for small motors up to several seconds for large motors.

Therefore, owing to the transient nature of the signal, conventional FFT analysis is not suitable for analysing starting currents. Although the short-time Fourier transform (STFT) can be used for analysing transient signals using a time–frequency representation, it can only analyse the signal with a fixed-sized window for all frequencies, which leads to poor frequency resolution. However, wavelet techniques can overcome this problem by using a variable-sized window.

Wavelet-based techniques for detecting broken rotor bars using the induction-motor starting current have been reported previously in [7] and [8]. Reference [7] uses an adaptive signal-cancellation technique to remove the fundamental component from the starting current, leaving only the residual current. This residual current is then analysed by using a discrete wavelet transform. The resultant

IEE Proceedings online no. 20060060

doi:10.1049/ip-epa:20060060

Paper first received 26th February and in final revised form 19th May 2006

R. Supangat, N. Ertugrul, W.L. Soong, D.A. Gray and J. Grieger are with Electrical and Electronic Engineering Department, University of Adelaide, Adelaide, Australia

C. Hansen is with Mechanical Engineering Department, University of Adelaide, Adelaide, Australia

E-mail: rsupang@eleceng.adelaide.edu.au

wavelet coefficients are then used to differentiate a healthy motor and a faulty motor under varying loading conditions. Reference [8] applies the wavelet transform to the Hilbert transform of the starting-current signal. The resultant wavelet coefficients are then used to compute what is called the wavelet ridge. This wavelet ridge is utilised to distinguish a healthy motor from a faulty motor with varying degrees of broken rotor bars.

Other transient-analysis techniques for monitoring of machines are reported in [9, 10]. Reference [9] shows a technique based on order tracking as the machine is run up to operating speed and back down to zero speed again. This method is primarily used in vibration analysis for reducing the smearing effect in the spectrum of a transient signal. The technique is implemented by using a speed sensor to control the signal-sampling rate, thus allowing reasonably long records to be taken as the machine is changing speed. However, such analysis is only useful for tracking faults which are characterised by frequency components that are proportional to the operating speed, because the sampling rate can only be synchronised to the motor speed. Owing to this limitation and the additional speed-sensor requirement, this technique is not considered in this study. In another study, reported in [10], it was suggested that broken-rotor-bar detection is possible by utilising the transient induced voltage on the stator windings of induction motors after a supply disconnection. In that method, it was assumed that the frequency of the induced voltage did not change significantly during the first few cycles of the signal measured; hence FFT techniques were implemented. The paper provides a comprehensive simulation study but presents only one set of experimental results to demonstrate the order of harmonics relevant to the broken-rotor-bar fault. This work did not investigate the effects of changes in loading, the number of broken rotor bars or the effect of varying the supply phase angle at disconnection.

This paper proposes a new method for detecting broken-rotor-bar faults under different loading conditions and varying fault severity. The method utilises a wavelet transform of the envelope of the starting current to distinguish between healthy and faulty motors.

2 Description of the wavelet methods

The wavelet transform is given by

$$C(a,\phi)=\int_{-\infty}^{\infty} f(t)\Psi(a,\phi,t)dt=\frac{1}{\sqrt{a}}\int_{-\infty}^{\infty} f(t)\Psi\left(\frac{t-\phi}{a}\right)dt \quad (1)$$

where C is the wavelet transform, a is the wavelet scale, ϕ is the wavelet position, $f(t)$ is the signal and Ψ is the wavelet function [11].

Equation (1) shows that the main concept of the wavelet transform is to divide a signal into its various scaled and shifted versions of a wavelet, in a similar fashion to the way the Fourier transform of a real variable divides a signal into its sinusoidal components of different frequencies with different or equal magnitudes and phases. A high-scale wavelet corresponds to a 'stretched' wavelet, which has a slow rate of change and hence low frequency. On the other hand, a low-scale wavelet corresponds to a 'compressed' wavelet with rapidly changing detail and hence high frequency. The wavelet function used for the analysis is 'db8' from the Daubechies family [11].

There are two types of wavelet analysis which can be used to analyse the induction-motor starting current: the continuous wavelet transform (CWT) and the discrete wavelet transform (DWT). The CWT utilises a continuous range of scales and shifts at the expense of increased computational time, whereas the DWT utilises a discrete range (in powers of 2) of scales and shifts. Since the CWT utilises a continuous range, it is easier to interpret the data than its DWT counterpart and hence the CWT is the technique used in this paper. Even though CWT is supposed to have a continuous range of scales and shifts, real computation cannot process continuous data. Therefore the CWT applied in this paper utilises integer multiples of scales and shifts. On the other hand, the DWT may be beneficial in practical applications because of the shorter computational time, which is of the order of $\log(m \times n)$ where n = number of scales and m = number of shifts.

A filtering interpretation of the wavelet transform is illustrated in Fig. 1. At each level, the signal is separated using low- and high-pass filters into a 'detail' component, which consists of the high-frequency components (in terms of the wavelet used), and an 'approximation' component, which consists of the low-frequency components (in terms of the wavelet used). The high-pass filter coefficients are the wavelet coefficients approximately scaled. The correlation between the signal and the wavelet at each level of scaling and for various time shifts is termed the wavelet coefficient.

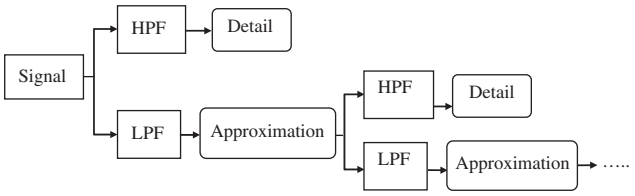

Fig. 1 *Multiple-level wavelet decomposition, where LPF and HPF are a low-pass filter and a high-pass filter, respectively, in terms of the wavelet used*

In this paper, the wavelet transform is applied to the induction-motor starting current and its envelope. The envelope of the signal, as will be explained below, provides additional information about the transient characteristics of the starting-current signal. Finally, the resulting wavelet coefficients are compared for different severities of broken rotor bars under various loading conditions.

2.1 Continuous wavelet transform (CWT) of the starting current

The wavelet technique permits the analysis of a transient signal, such as the starting current of an induction motor, where a normal FFT would not be beneficial. The continuous wavelet transform (CWT) can be utilised to extract and analyse the transient characteristics of the starting current of an induction motor. Figure 2 shows an example where the CWT has successfully extracted the transient characteristics of typical starting-current waveforms, which were obtained using the test setup described in Section 3. The CWT has distinguished the differences, which are faintly visible in the wavelet plots, between the healthy and faulty motors.

Figure 2 suggests that there are two evident effects of the broken-rotor-bar fault on the starting current. The first effect is that the starting current takes a longer time to decay and reach steady state compared with to a healthy induction motor. This is because an induction motor with broken rotor bars produces less torque and hence takes longer to reach steady state. However, this effect cannot be used as a feature for distinguishing healthy and faulty motors because it can also be caused by changes in the inertia and the

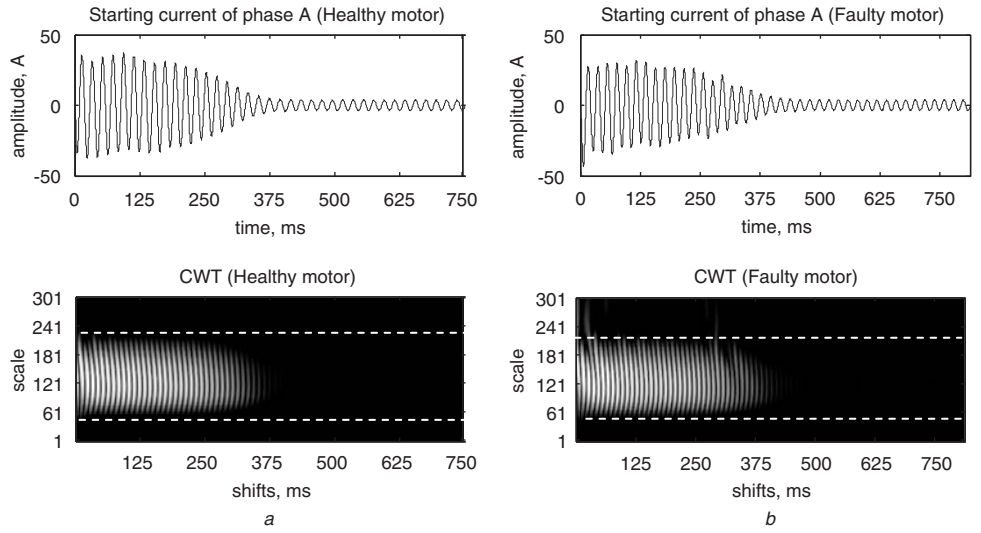

Fig. 2 *Healthy and faulty motors running at no load*
Top: Starting-current signal sampled at 8 kHz
Bottom: Continuous-wave transform of the original signal with 50 Hz component
a Healthy motor
b Faulty motor with four broken rotor bars

loading conditions of the motor. The second effect is apparent in the CWT plots. There are observable differences between the CWT plot of a healthy motor and the CWT plot of a faulty motor with four broken rotor bars (Fig. 2) at shifts around 0–375 ms, which correspond to the starting period, and scales around 200–301, which correspond to lower-frequency components, where the wavelet coefficients of the faulty motor are stronger than the wavelet coefficients of the healthy motor. These differences indicate that the wavelet transform is able to detect the changes in signal components between the faulty motor and the healthy motor during the starting period, and are suggested to be the identifying feature for detecting a broken-rotor-bar fault. However, the differences are overshadowed by the strong fundamental 50 Hz component in the signal (as highlighted by the region between the dashed lines in the Figures), which does not incorporate any useful information about rotor-bar faults. Therefore, this 50 Hz component needs to be removed in order to have a more accurate and reliable analysis.

2.2 Continuous wavelet transform (CWT) of the envelope of the starting current

To remove the fundamental component, a signal model for the stator current is required. Here, it is suggested that the stator-current signal is a summation of many modulated signal components and other fundamental components, such as the supply frequency, the rotor frequency and the slip frequency. This suggestion is supported in [3], which indicates that most of the fault frequencies are symmetrical about certain frequencies. For example, the broken-rotor-bar (BRB) fault frequencies, $f \pm 2sf$ (where f is the fundamental frequency and s is the slip), are symmetrical about the fundamental frequency.

Let $i(t)$ denote the steady-state stator current which comprises many modulated signal components:

$$i(t) = i_s(t) + n(t) \tag{2}$$

where $i_s(t)$ is the steady-state signal components and $n(t)$ represents the noise components.

The steady-state signal component $i_s(t)$ can be divided into simpler signal components by the principle of superposition. In this paper, the signal components of interest are the BRB sidebands. Therefore the signal component, $i_s(t)$, is defined as in (3):

$$i_s(t) = i_{s1}(t) + i_{so}(t) \tag{3}$$

where $i_{s1}(t)$ is the steady-state BRB sideband modulated at the fundamental frequency, and $i_{so}(t)$ represents the other steady-state signal components that make up the stator current.

In this case, let the fundamental signal component i_f and the BRB component i_{brb} be defined as in (4) and (5), respectively:

$$i_f(t) = a_f \cos(\omega_f t) \tag{4}$$

$$i_{brb}(t) = a_{brb} \cos(\omega_{brb} t) \tag{5}$$

where a_f and a_{brb} are the amplitudes of the fundamental signal component and the BRB component, respectively. Therefore, the steady-state BRB sideband modulated at the fundamental frequency $i_{s1}(t)$ is given in (6) [2, 3, 5]. In this case, the fundamental signal component i_f acts as a carrier, which modulates the BRB component. In terms of the frequency domain, the BRB component is shifted from the baseband to the carrier-signal frequency:

$$\left.\begin{aligned} i_{s1}(t) &= \{a_f + a_{brb}\cos(\omega_{brb}t)\}\cos(\omega_f t) \\ &= a_f \cos(\omega_f t) + \frac{a_{brb}}{2}\cos\{(\omega_f + \omega_{brb})t\} \\ &\quad + \frac{a_{brb}}{2}\cos\{(\omega_f - \omega_{brb})t\} \end{aligned}\right\} \tag{6}$$

The above equation shows that the sum of a_f and a_{brb} is proportional to the amplitude of the current component. As can be seen in Fig. 2, this sum is significantly larger during the starting period than during the steady-state operation. Therefore, the BRB sidebands should be more detectable during the starting period. In addition, note that owing to the time-varying feature of the starting current, some variables in (6) are also time varying, such as $a_f = a_f(t)$, $a_{brb} = a_{brb}(t)$, and $\omega_{brb}(t) = 4\pi s(t) f$, where $s(t)$ is the time-varying slip.

The method used to remove the fundamental component $i_f(t)$ is through demodulation, which is equivalent to extracting the envelope of the starting current. The demodulation-process flow diagram and its mathematical

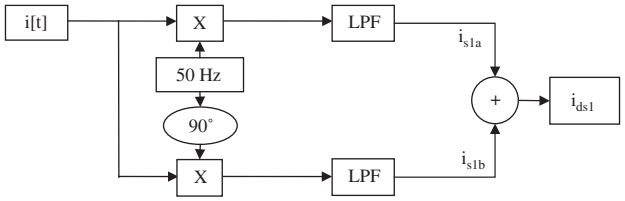

Fig. 3 *Implementation flow diagram of the envelope extraction*

formulation are shown in Fig. 3 and (7)–(9), respectively. The demodulation process shows that the starting current signal $i[t]$ is multiplied by cosine and sine 50 Hz sinusoids. This fundamental frequency can be estimated using the data to allow for variations in the actual frequency. Then, the resulting real and quadrature components i_{s1a} and i_{s1b} respectively, are filtered separately. Finally, the magnitude of the sum i_{ds1} of the real and quadrature components gives the envelope of the signal.

Let $i_{ds1}(t)$ be the output of the demodulation process and let LPF be the low-pass filtering process. Then

$$i_{ds1}(t) = \mathrm{LPF}(i_{s1a} + ji_{s1b}) \tag{7}$$

where

$$\left.\begin{aligned} i_{s1a}(t) &= \frac{a_f}{2} + \frac{a_f}{2}\cos(2\omega_f t) + \frac{a_{brb}}{4}\cos\{(2\omega_f + \omega_{brb})t\} \\ &\quad + \frac{a_{brb}}{4}\cos(\omega_{brb}t) + \frac{a_{brb}}{4}\cos\{(2\omega_f - \omega_{brb})t\} \\ &\quad + \frac{a_{brb}}{4}\cos(\omega_{brb}t) \\ i_{s1b}(t) &= \frac{a_f}{2}\sin(2\omega_f t) + \frac{a_{brb}}{4}\sin\{(2\omega_f + \omega_{brb})t\} \\ &\quad + \frac{a_{brb}}{4}\sin(\omega_{brb}t) \\ &\quad + \frac{a_{brb}}{4}\sin\{(2\omega_f - \omega_{brb})t\} - \frac{a_{brb}}{4}\sin(\omega_{brb}t) \end{aligned}\right\} \tag{8}$$

and hence

$$\begin{aligned} i_{ds1}(t) &= \frac{a_f}{2} + \frac{a_{brb}}{2}\cos(\omega_{brb}t) \\ &= \frac{1}{2}\{a_f + a_{brb}\cos(\omega_{brb}t)\} \end{aligned} \tag{9}$$

Equation (9) clearly shows that the demodulation process has successfully removed the fundamental signal component $i_f = a_f \cos(\omega_f t)$, leaving a DC component and the BRB component. The sum of $i_{so}(t)$ these components and the other signal components corresponds to the envelope of the starting-current signal.

Figure 4 shows the improvement obtained by applying the continuous wavelet transform (CWT) on the envelope of the starting-current signal compared with applying it on the signal itself. It shows that, by applying the CWT on the envelope, the fundamental 50 Hz component has been removed successfully. As a result, a more accurate and precise transient analysis can be performed and investigated. Note that this process has also been tested on the other current phases where similar results are obtained (see Section 3.2).

Figure 4 reveals another effect of a broken-rotor fault. The effect can be seen from the starting-current-envelope plots, in which the faulty motor draws slightly less current than the healthy motor during starting. This is because there are effectively fewer rotor bars and hence less torque in the faulty motor.

Further examination of the CWT plots in Fig. 4 reveals the differences between the healthy motor and the faulty motor with broken rotor bars. To analyse these differences accurately, the CWT plots are divided into three different time regions (regions 1, 2, and 3, separated by the dashed lines) for identifying the different patterns. The regions were initially identified through visual inspection of the starting-current waveform and its wavelet transform. However, further experiments show that the lines separating the regions are found to be located consistently with respect to the starting-current waveform.

The starting current of a healthy motor exhibits two distinct patterns under the wavelet analysis (Fig. 4), where

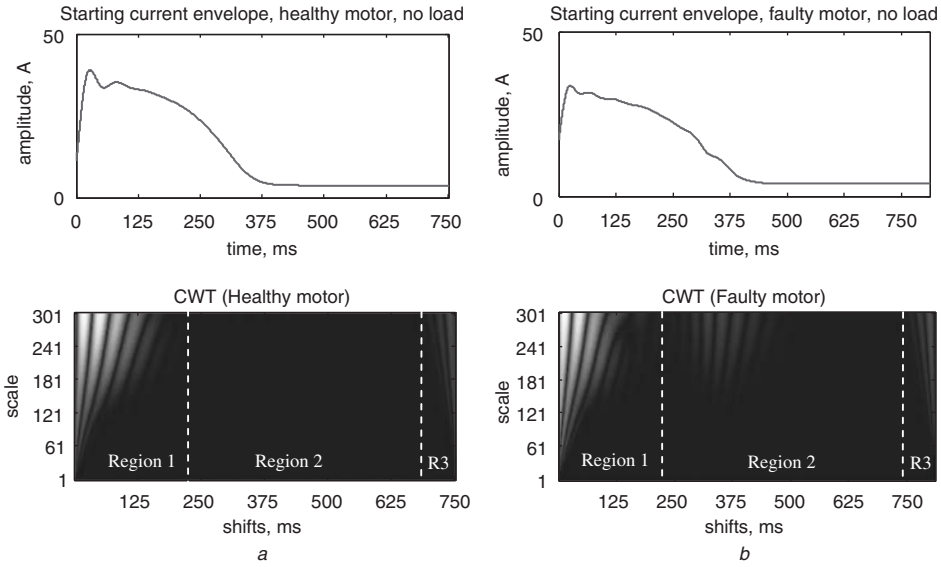

Fig. 4 *Envelope and continuous wavelet transform of the starting current shown in Fig. 2 after 50 Hz component is removed*
Top: Envelope
Bottom: Continuous wavelet transform
a Healthy motor
b Faulty motor with four broken rotor-bars

the first pattern (in region 1) corresponds to the initial part of the envelope and the second pattern (in region 3) corresponds to the end (discontinuity) of the signal. On the other hand, a faulty motor with broken rotor bars exhibits an extra pattern between these two patterns (in region 2), which occurs just before the transition from the 'starting state' to the steady state. This pattern is named the 'third pattern' in this paper and is the distinguishing feature between a healthy and a faulty motor. Although there is a small difference in the first pattern (in region 1) between the healthy and faulty motors, it was found to be difficult to detect and hence will not be considered in this paper.

2.3 Wavelet indicator

The differences between the patterns of a healthy motor and the patterns of a faulty motor with broken bars need to be quantified for more convenient identification and possible use in a future automated condition-monitoring system. These pattern differences may be quantified by calculating the sum of all the absolute values of the wavelet coefficients in the third pattern (in region 2). The resultant value is then normalised against the sum of all the wavelet coefficients, the number of samples used and the number of scales used. In this paper, the power magnitude of the square of this quantification value is termed the 'wavelet indicator'.

Figure 5 shows that the wavelet indicator has successfully quantified the pattern differences and hence distinguished a faulty motor with broken rotor bars from a healthy one. The wavelet indicator of a faulty motor with 4 broken rotor bars (4 BRB) is consistently higher than the wavelet indicator of a healthy motor under various loading conditions. This finding shows a significant improvement over steady-state analysis methods, such as FFT analysis, where the fault detection is dependent on the loading conditions (i.e. the fault detection is inaccurate at light load).

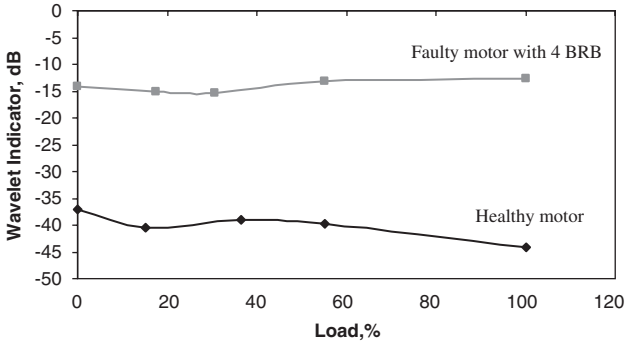

Fig. 5 *Wavelet-indicator plot of the starting current for various loading conditions for a healthy motor and for a faulty motor with four broken rotor bars*

3 Experimental results

The experimental results given below were obtained using a purpose-built test rig based on a high-speed data-acquisition system (two DAQPAD-6052E boards from National Instruments, capable of simultaneous sampling at 5 MHz) with custom-written LabVIEW software. A number of identical 2.2 kW, 415 V, 4-pole, 32-rotor-bar, star-connected induction motors were used in this test. The motors were loaded by a separately excited 5 kW DC generator. The motors were installed on the test rig using a precision laser alignment tool and a torque wrench to ensure the accuracy and the repeatability of the data obtained. During the test, two current sensors, for measuring two phase currents, were attached to the motor, and the sensor outputs were sampled simultaneously at 8 kHz via an antialiasing filter, which was an 8th-order Butterworth filter, with a cut-off frequency of 2 kHz.

Experimental data of the motor starting currents were collected using healthy motors, healthy motors with an unbalanced supply and faulty motors with varying degrees of broken bars. An unbalanced supply is simulated by inserting a resistor in series with one of the supply phases.

The profile of the rotor bars in the test machine can be seen in Fig. 6*a*, where a section of the rotor end ring has been cut completely away. Broken-rotor-bar faults were simulated by cutting a narrow slot through the end ring next to the lamination stack using a small-diameter milling cutter to break the electrical connection between the rotor bar and end ring. This method is used to minimise the disturbance to rotor-end-ring currents which would occur if the end ring were removed as in Fig. 6*a*. A partial broken-rotor-bar fault is created by decreasing the depth of the slot to remove only a portion of the rotor-bar cross-sectional area. For example, a 25% broken rotor bar means that 25% of the rotor bar's cross-sectional area is removed (Fig. 6*b*).

A separately-excited DC machine with a resistive load was used to load the test machine. This produced a load torque which varied approximately linearly with motor speed. For instance, when the machine was started at full load, the load torque only reached its rated value when the machine reached rated speed. The percentage load given in Figs. 6–8 was estimated using the slip of the machine after the motor reached steady-state operation. Figure 6*c* shows the starting-current variations between the no-load case and the full-load case. As expected, the increase on the load causes the starting time of the motor running at full load to be about 100 ms longer than that for the motor running at no load.

The experimental data, which are the starting current of the induction motors sampled at 8 kHz, were then analysed using the wavelet technique described in Section 2. To show that the wavelet technique can be used reliably for detecting broken-rotor-bar faults, it is necessary to show experimentally that:

(*a*) the measurements are repeatable,

(*b*) the changes in the wavelet coefficients due to broken rotor bars are not sensitive to effects such as motor loading, initial rotor position and supply imbalance, and

(*c*) the wavelet technique is able to distinguish between various degrees of broken-rotor-bar fault.

3.1 Variability of the test set-up and the wavelet technique

There are two types of variability tests considered in this paper. First, the variability of the motor set-up, which is performed to ensure that the measurements obtained are repeatable, and secondly the variability of the wavelet technique under different loading conditions, initial rotor positions and initial phase angle of the supply. The wavelet-technique-variability test is required to ensure that the pattern differences between the healthy and faulty motors (with broken rotor bars) are caused by the broken-rotor-bar fault and are not affected by loading conditions, initial rotor position or the initial phase angle of the supply. For instance, the wavelet technique needs to be able to distinguish between the acceleration characteristic due to

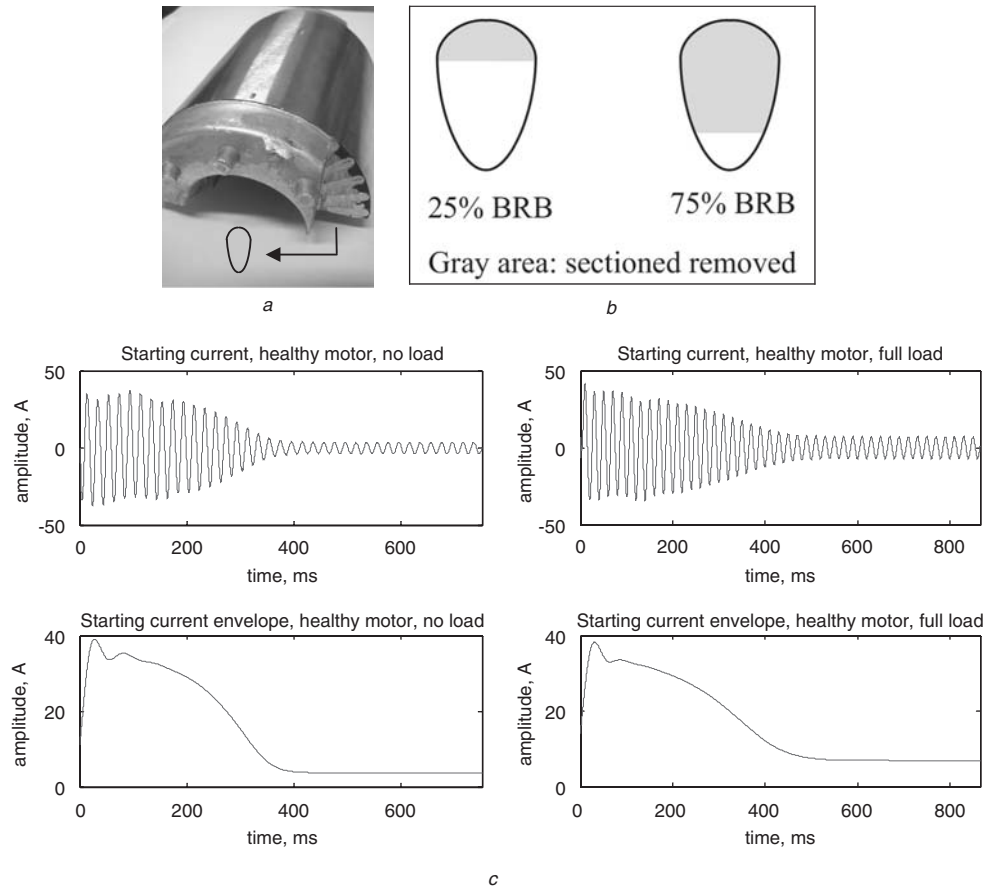

Fig. 6 *Photograph of the rotor cross-section showing the profile of the rotor bars and starting-current characteristics at no load and full load*
a Photograph
b Cross-section of profile
c Starting-current characteristics

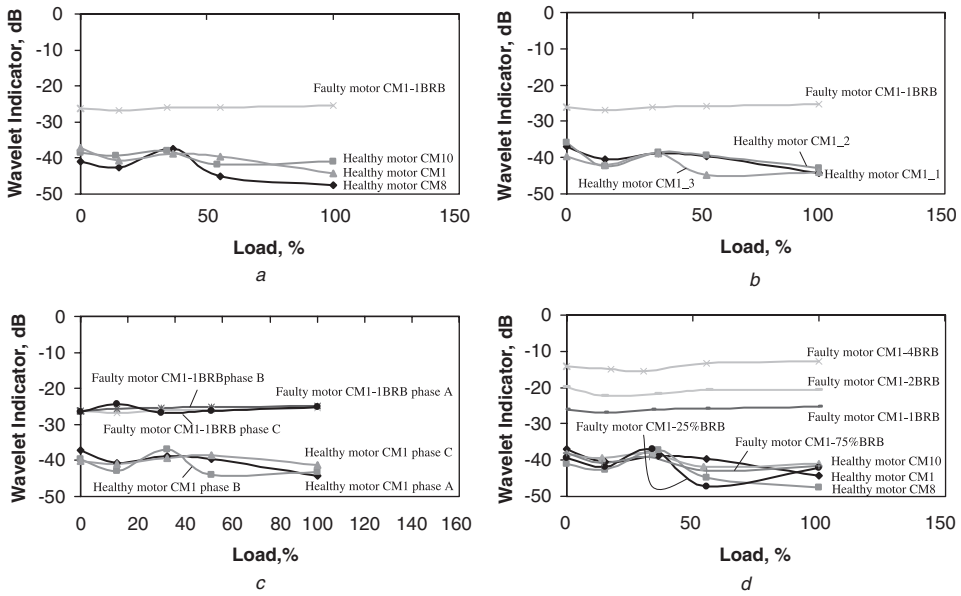

Fig. 7 *Wavelet-indicator plot as a function of load, for the starting current*
a Three healthy motors (CM_1, CM_8, CM_{10}) and one faulty motor with a broken rotor bar (1BRB)
b Healthy motor with different initial rotor position and supply phases
c Three different current phases of a healthy motor
d All motors tested

broken rotor bars on an unloaded machine and, say, the acceleration characteristic of a healthy machine starting under load.

Figure 7*a* shows the variability of the measurements for three different healthy motors, namely motors CM_1, CM_8 and CM_{10}. As shown by Fig. 7, the three wavelet indicator lines are very close to each other, which indicates a small degree of variability of the measurement data between the different healthy machines. Also, note that the wavelet indicator lines for the healthy motors are well below the

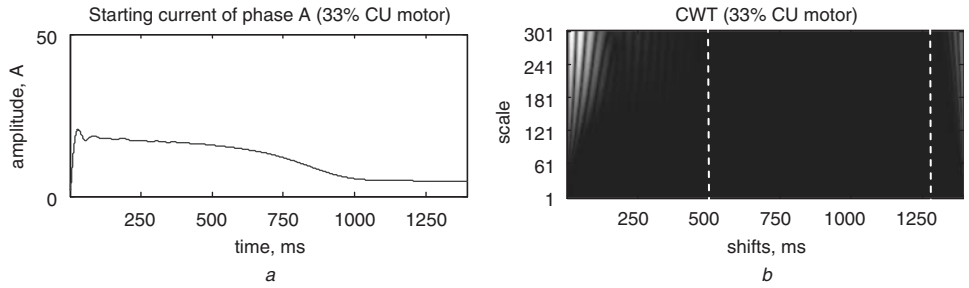

Fig. 8 *Envelope and Continuous Wavelet transform of the starting current for a motor with 33% of current unbalance*
a Envelop
b Continuous wavelet transform

lowest level obtained for the faulty machine. Therefore, the slight variability between the healthy motors is insignificant.

The wavelet-indicator plots in Fig. 7*b* indicate how the loading response of the wavelet indicator changes with different initial rotor positions and different phases angles of the supply voltage at starting. This variability test is done on a healthy motor (CM_1) and is repeated three times by choosing random initial rotor positions and starting phases angles of the supply voltage for every test and every loading condition. As shown in Fig. 7*b*, the three wavelet indicator lines are close to each other, which indicates that the results from the wavelet technique are not very sensitive to the loading conditions, initial rotor position, and the phase angle of the supply voltage at starting. Therefore, it can be concluded that any changes to the wavelet indicator exhibited by a faulty motor with broken rotor bars can only be caused by the broken-rotor-bar fault.

Figures 7*a* and 7*b* also show a general trend of the wavelet indicator plots for healthy motors, where they tend to decrease slightly as the load increases.

3.2 Variability between the different current phases

The wavelet-indicator plot in Fig. 7*c* is given to show the variability between the current signals in each of the three phases of the motor. The Figure shows that the wavelet-indicator variability between the different phases is relatively small (less than 5 dB) compared with the differences between the wavelet indicators of a healthy motor and a faulty motor with one broken rotor bar (approximately 15 dB). This variability test confirms that the wavelet characteristics, which are explained in the previous Sections, are consistent in all of the current phases and that the differences between the three phases are insignificant. Therefore, it is justified to consider only one phase of the current for the analysis.

3.3 Comparison and classification of healthy and faulty motors

As stated above, the wavelet indicator is proposed as a means of comparing healthy and faulty motors (with broken rotor bars) and classifying the various degrees of broken-rotor-bar fault. The comparison and classification is done by measuring the magnitude of the wavelet indicator, and is given in Fig. 7*d*.

Figure 7*d* clearly shows that the wavelet indicators of faulty motors with broken rotor bars are consistently higher than the wavelet indicators of healthy motors. The reason for this increase is due to the broken rotor bar 'third pattern' that emerges in the wavelet transform of the envelope of the starting current for motors with a broken-rotor-bar fault but not in healthy motors. Note also that the third wavelet pattern changes its scale and position depending on the loading conditions, such that, the higher the load, the higher is the scale and the further is the position, but it always lies between the first and the second wavelet pattern. This pattern behaviour and the fact that the magnitude of the BRB sidebands varies with load accounts for the variability between the wavelet indicators of the healthy motors (Figs. 7*a–b*).

Figure 7*d* also shows a general trend of the wavelet-indicator lines for the faulty motors, where they tend to increase slightly as the load increases. This trend characteristic of the faulty motors is significantly different from the trend characteristic of the healthy motors, where the wavelet indicator lines tend to decrease with increasing load. Hence, distinguishing between the two characteristics is made easier if the motor can be started with varying levels of load.

Another trend observable in Fig. 7*d* is that the wavelet indicator increases as the severity of the broken-rotor-bar fault increases. As we can see from Fig. 7*d*, the faulty motor with four broken bars has the highest wavelet indicator. This is then followed by the wavelet indicator of the faulty motor with two broken rotor bars, followed by the faulty motor with one broken rotor bar. In addition, this trend is consistent under different loading conditions. Hence, classifying different severities of the fault appears simple, at least for fully broken-rotor-bars.

The wavelet indicators for the motors with a 25% and 75% partially broken rotor bar are very close to those of the healthy motors, and hence it is difficult to distinguish these two cases from the healthy machines. The reason for this is that a partially broken rotor bar is likely to produce only a small change in the overall bar resistance and hence has little effect on the current distribution in the rotor [6].

3.4 Motors with unbalanced supplies

Motors with unbalanced supplies show different wavelet characteristics from that of motors with broken-rotor-bar faults. They do not produce an extra wavelet pattern between the first and the second wavelet patterns, like motors with broken-rotor-bar faults do, but rather slightly alter and extend the first wavelet pattern. This characteristic is shown in Fig. 8*a*, which displays the plot of a wavelet-envelope analysis on a motor with 33% of current unbalance and 7.1% of voltage unbalance. The unbalance factor is calculated based on the full-load steady-state signals according to the equations given in (10) and (11) for the voltage only:

$$UF = \frac{\max(|V_{a(rms)} - V_{avg}|, |V_{b(rms)} - V_{avg}|, |V_{c(rms)} - V_{avg}|)}{V_{avg}} \quad (10)$$

$$V_{avg} = \frac{(V_{a(rms)} + V_{b(rms)} + V_{b(rms)})}{3} \quad (11)$$

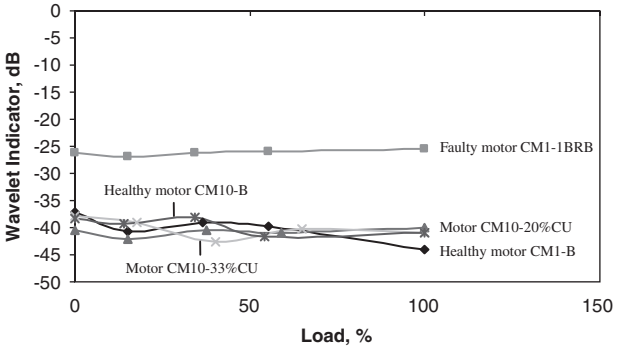

Fig. 9 *Wavelet-indicator plot for healthy and faulty motors*
CU = current unbalanced
B = balanaced

where UF is the unbalanced factor; $V_{a(rms)}$, $V_{b(rms)}$, $V_{c(rms)}$ are the RMS values of the three phase voltages of the motor; and V_{avg} is the average value of these three voltages.

In Fig. 9, the wavelet indicators for the motors with 33% and 20% of current unbalance are about the same level as for the healthy-motor case. This result shows that the wavelet indicator is not affected by an unbalance in the supply. Therefore the proposed wavelet technique is reliable in detecting broken-rotor-bar faults even if the motor has an unbalanced supply.

4 Conclusions

This paper has investigated the detection of broken rotor bars using wavelet analysis of the starting current. The wavelet technique presented here is able to extract useful characteristics from the starting current of an induction motor, and can distinguish healthy and faulty motors by means of a numerical value called the wavelet indicator. Further, the wavelet indicator can also be used to classify the different levels of severity of broken-rotor-bar faults. It was found that the higher the value of the wavelet indicator, the greater the severity of the fault. However, it was observed that partially broken rotor bars in the test machine cannot be detected using this method. This is likely to be due to the small size of the motor under test and the minimal resistance changes caused by a partially broken rotor bar.

The proposed technique, using the wavelet indicator, is able to distinguish faulty motors from healthy ones and classify the different levels of severity of the fault irrespective of the loading conditions. In addition, the wavelet technique has also been shown to be reliable and unaffected by various other factors such as initial rotor position, phase angle of the supply voltage at starting and supply imbalance.

5 Acknowledgment

The authors acknowledge the valuable support provided by National Instruments Corporation, USA and the assistance provided by the workshop staff in the School of Electrical and Electronic Engineering.

6 References

1 Ahmed, I., Supangat, R., Grieger, J., Ertugrul, N., and Soong, W.L.: 'A baseline study for on-line condition monitoring of induction machines'. Australasian Universities Power Engineering Conf., AUPEC, Brisbane, Australia, 2004
2 Bellini, A., Filippetti, F., Franceschini, G., Tassoni, C., and Kliman, G.B.: 'Quantitative evaluation of induction motor broken bars by means of electrical signature analysis', *IEEE Trans. Ind. Appl.*, 2001, **37**, pp. 1248–55
3 Benbouzid, M.E.H.: 'A review of induction motor signature analysis as a medium for faults detection', *IEEE Trans. Ind. Electron.*, 2000, **47**, (5), pp. 984–993
4 Kliman, G.B., Premerlani, W.J., Yazici, B., Koegl, R.A., and Mazereeuw, J.: 'Sensorless, online motor diagnostics', *IEEE Comput. Appl. Power*, 1997, pp. 39–43
5 Nandi, S., and Toliyat, H.A.: 'Condition monitoring and fault diagnosis of electrical machines—a review'. IEEE Industrial Applications Soc. Ann. Meet., 1999
6 Siau, J., Graff, A., Soong, W.L., and Ertugrul, N.: 'Broken bar detection in induction motors using current and flux spectral analysis', *Aust. J. Electr. Electron. Eng.*, 2004, **1**, (3), pp. 171–177
7 Douglas, H., Pillay, P., and Ziarani, A.K.: 'A new algorithm for transient motor current signature analysis using wavelets', *IEEE Trans. Ind. Appl.*, 2004, **40**, (5), pp. 1361–1368
8 Zhang, Z., Ren, Z., and Huang, W.: 'A novel detection method of motor broken rotor bars based on wavelet ridge', *IEEE Trans. Energy Conv.*, 2003, **18**, (3), pp. 417–423
9 Xu, M.: 'Orders tracking analysis of variable speed machines'. Proc. 1998 Enteract International: Information through Integration, Cincinnati, Ohio, 1998
10 Milimonfared, J., Kelk, H.M., Nandi, S., Minassians, A.D., and Toliyat, H.A.: 'A novel approach for broken rotor bar detection in cage induction motors', *IEEE Trans. Ind. Appl.*, 1999, **35**, (5), pp. 1000–1006
11 Daubechies, I.: 'The wavelet transform, time-frequency localization and signal analysis', *IEEE Trans. Inf. Theory*, 1990, **36**, pp. 961–1005